Differential Near-Field Scanning Optical Microscopy Using Sensor Arrays

Aydogan Ozcan, *Member, IEEE*, Ertugrul Cubukcu, *Student Member, IEEE*, Alberto Bilenca, *Member, IEEE*, Brett E. Bouma, Federico Capasso, *Fellow, IEEE*, and Guillermo J. Tearney

(Invited Paper)

***Abstract*—In this paper, we introduce a new aperture-type near-field scanning optical microscopy (NSOM) imaging concept that relies on specially designed large-area (e.g., $>$200 nm $\times$ 200 nm) aperture geometries having sharp corners. Unlike in conventional NSOM, the spatial resolution of this near-field imaging modality is not determined by the size of the aperture, but rather by the sharpness of the corners of the large aperture. This approach significantly improves the light throughput of the near-field probe and, hence, increases the SNR. Here, we discuss the basic concepts of this near-field microscopy approach and illustrate both theoretically and experimentally how an array of detectors can be utilized to further improve the SNR of the near-field image. The results of this work are particularly relevant for imaging of biological samples at a spatial resolution of $<$50 nm with significantly improved image quality.**

***Index Terms*—Differential NSOM (DNSOM), near-field imaging, near-field scanning optical microscopy (NSOM), SNOM.**

I. Introduction

In OPTICAL microscopy, the diffraction limit prevents imaging with a spatial resolution better than half a wavelength of light. Overcoming this limitation of optical microscopy has been the subject of much research over the past two decades [1]–[21]. As a result of these efforts, near-field scanning optical microscopy (NSOM) has been demonstrated as a promising imaging modality that permits superresolution imaging of samples (fluorescently labeled or not) by breaking the diffraction barrier of light [2]–[14]. NSOM can achieve a spatial resolution of $<\sim$100 nm under room temperature without any vacuum requirements, and provides a unique nondestructive optical alternative to electron microscopy. Such a high optical resolution is especially important for applications, such as single-molecule imaging/spectroscopy, cell membrane protein imaging, or even rapid DNA mapping [22]–[31].

In conventional aperture-type NSOM, a small aperture probe (with a diameter of $<\sim$100 nm) is scanned in the near-field (i.e., within $<\sim$20 nm away from the surface) of the object to be imaged, using an active closed-loop feedback, such as shear force feedback. The function of the small-aperture probe is either to collect the transmitted (or reflected) light from a small spot on the sample or to illuminate the sample. In either case, the detection of photons is done in the far-field, through a diffraction-limited imaging system. A 2-D NSOM image is formed by scanning the NSOM probe (or the sample) while a sensitive optical detector located in the far-field (e.g., a photomultiplier tube or an avalanche photodiode) is counting photons as a function of the scanning position.

The spatial resolution of such aperture-type NSOM systems is limited roughly by the aperture size of the probe [5]. Typically, a probe diameter of $\sim$80–100 nm is used, which yields a spatial resolution of $\sim$100–120 nm. However, since the effective transmission (i.e., the light throughput) decreases as the 6th power of the aperture diameter [32]–[34], improved resolution (e.g., using a smaller aperture probe with $<$50-nm diameter) comes at the price of a sharp decrease in SNR and contrast of the NSOM image. Furthermore, the effective diameter of the aperture in conventional aperture-type NSOM cannot be physically smaller than twice the skin depth of the metal tip, which implies a lower bound of $\approx$15–20 nm for the *effective* aperture width.

To address some of these issues associated with the aperture-type NSOM, a scattering-type apertureless NSOM has also been successfully demonstrated as a promising near-field imaging modality [5], [21], [35]–[38]. In this approach, a sharp tip [e.g., a regular atomic force microscope (AFM) tip] locally scatters the near-field photons of an object into a far-field detector. Since the sharpness of the probe can be made extremely small, this scattering process can, in principle, yield very high spatial resolution imaging of the near-field of an object. However, apertureless NSOM systems are harder to align and operate since they require an intensity enhancement of $>$1000–2000

Manuscript received September 24, 2007. This work was supported in part by the Department of Defense, Medical Free Electron Laser Program under Grant FA9550-04-1-0079, and in part by the Center for Nanoscale Systems at Harvard University. The work of A. Ozcan was supported by the Center for Nanoscience Innovation for Defense at the University of California, Los Angeles. The work of E. Cubukcu was supported by the Air Force Office of Scientific Research under a Multidisciplinary University Research Initiative Program. The work of F. Capasso was supported by the Air Force Office of Scientific Research under a Multidisciplinary University Research Initiative Program.

A. Ozcan is with the Department of Electrical Engineering, University of California, Los Angeles, CA 90095 USA, and also with the Biomedical Engineering IDP, University of California, Los Angeles, CA 90095 USA. All Correspondence should be addressed to A. Ozcan (e-mail: ozcan@ucla.edu).

E. Cubukcu and F. Capasso are with the School of Engineering and Applied Sciences, Harvard University, Cambridge, MA 02138 USA.

A. Bilenca is with the Harvard Medical School, Boston, MA 02114 USA.

B. E. Bouma is with the Harvard Medical School, Boston, MA 02114 USA, and also with the Harvard-MIT Division of Health Sciences and Technology, Cambridge, MA 02139 USA.

G. J. Tearney is with the Harvard Medical School, Boston, MA 02114 USA, and also with Wellman Center for Photomedicine, Massachusetts General Hospital, Boston, MA 02114 USA.

Color versions of one or more of the figures in this paper are available online at http://ieeexplore.ieee.org.

Digital Object Identifier 10.1109/JSTQE.2007.910799

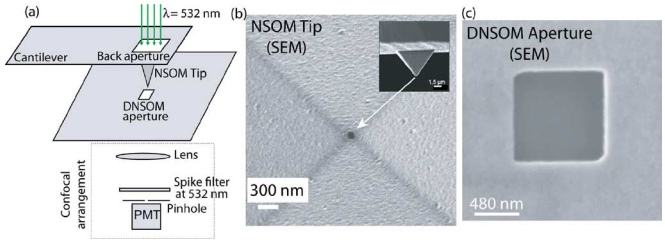

Fig. 1. (a) Proof-of-principle DNSOM experimental setup, where far-field detection is achieved using a photomultiplier tube (PMT). (b) SEM picture of a 100-nm-wide NSOM tip used in the experiment. (c) SEM picture of a DNSOM square aperture that is used in this proof-principle experiment.

at the tip in order to achieve reasonable contrast in the far-field. This is partially the reason why most of the currently existing commercial NSOM systems are based on an aperture probe.

In summary, the NSOM offers many unique features that have great potential for high-resolution bioimaging applications. However, today's state of the art for aperture-type NSOM has SNR and contrast issues for achieving an ultrahigh spatial resolution of <50 nm routinely, on a day-to-day basis. To address this issue of aperture-type NSOM systems, in prior work [39], [40] we introduced an alternative approach for aperture-type NSOM, termed *differential near-field scanning optical microscopy* (DNSOM). DNSOM involves scanning a relatively large square aperture [see, e.g., Fig. 1(c)] or a detector in the near-field of the object of interest, and recording the power of the light collected from the square structure as a function of the scanning position, as illustrated in Fig. 1(a). Image reconstruction in the DNSOM is achieved by taking a 2-D spatial derivative of the recorded power map. In contrast with conventional aperture-type NSOM, the size of the DNSOM aperture does *not* determine the resolution of the recovered image. In DNSOM, the resolution is, instead, determined by the sharpness of the corners of the square structure. This feature of the DNSOM allows the SNR of the near-field image to be significantly increased (e.g., by ~100 dB) without sacrificing resolution, which should enable near-field optical microscopy with <50-nm spatial resolution.

In this paper, we give a detailed analysis of the concept of DNSOM and introduce an improved DNSOM system, which uses instead of a single photon counting detector, an *array* of detectors. This improved DNSOM system is termed *DNSOM Multiplexed* (DNSOM^2) as it captures multiple images of the interaction of the DNSOM probe with the object of interest. DNSOM^2 increases the SNR of the near-field image by, e.g., ~25-fold when compared to the DNSOM. This SNR improvement of DNSOM^2 over DNSOM is qualitatively quite similar to the improved SNR performance of frequency-domain optical coherence tomography (OCT) systems over time-domain OCT systems [41]–[45].

This paper is organized as follows: In Section II, the basic concept of DNSOM is reviewed both theoretically and experimentally. Following this, in Section III, DNSOM^2 is introduced and verified with a proof-of-principle experiment. Finally, Section IV discusses some additional design issues related to further improving the performance of DNSOM and DNSOM^2.

II. An Alternative Near-Field Microscope: DNSOM

A. Theoretical Background of the DNSOM

In order to introduce the concept of the DNSOM, we model the optical power transmissivity of the 2-D object of interest by $O(x, y)$, where x and y denote the coordinates in the plane of the sample. The same derivation could also be extended to a reflection geometry rather than transmission. For this derivation, we will assume the object to be infinitely thin. This assumption is also made in other aperture-type or apertureless NSOM approaches making NSOM primarily a 2-D imaging modality. For our DNSOM derivation, let us further assume that, without loss of generality, the DNSOM aperture is a square with a width of W, i.e., the power transmissivity of the square aperture is given by: $\text{Rect}(x, y) = \{1, \quad \text{if } W/2 > |x| \quad \text{and } W/2 > |y|; \qquad 0 \text{ elsewhere}\}$. In this formulation, the effect of the skin depth at the walls of the square aperture has been ignored, an omission that will be addressed in the discussion to follow. Here, we should emphasize that this same analysis could also be extended to rectangular or triangular apertures that have sharp corners. For a scanning step size of Δx and Δy along x and y, respectively, the detected power in the far-field [through a numerical aperture (NA), e.g., $0.2 < \text{NA} < 1.4$) as a function of the scanning coordinates, $m \cdot \Delta x,\ n \cdot \Delta y$ (where m and n are integers) can be written as

$$P(m \cdot \Delta x, n \cdot \Delta y) = \iint [0(x, y) \cdot \text{Rect}(x - m \cdot \Delta x, y - n \cdot \Delta y)] \otimes h(x, y) \cdot dx \cdot dy \tag{1}$$

where "$\otimes$" denotes the spatial convolution operation and $h(x, y)$ is the 2-D point-spread function of the far-field imaging system that collects the transmitted (or reflected) light originating from the DNSOM aperture. In (1), we have assumed spatial incoherence for the far-field detection, which is valid especially for fluorescently labeled sample imaging. The entire analysis can easily be extended to coherent or partially coherent imaging systems without changing the end results. Furthermore, similar to conventional NSOM, we also assume in (1) that the probe is a passive probe, i.e., its interaction with the near-field image of the object is negligible.

By a simple change of variables, $x' = m \cdot \Delta x$ and $y' = n \cdot \Delta y$, one can take the 2-D spatial derivative of (1), and, after some algebraic steps, arrive at

$$\frac{\partial^2 P(x', y')}{\partial x' \cdot \partial y'} = \frac{2 \cdot NA}{\lambda} \cdot \begin{bmatrix} O(x' - W/2,\ y' - W/2) \\ +O(x' + W/2,\ y' + W/2) \\ -O(x' + W/2,\ y' - W/2) \\ -O(x' - W/2,\ y' + W/2) \end{bmatrix} \tag{2}$$

where, λ is the illumination wavelength, as illustrated in Fig. 1(a). Equation (2) indicates that by taking a 2-D spatial derivative of the scanning power output of the square

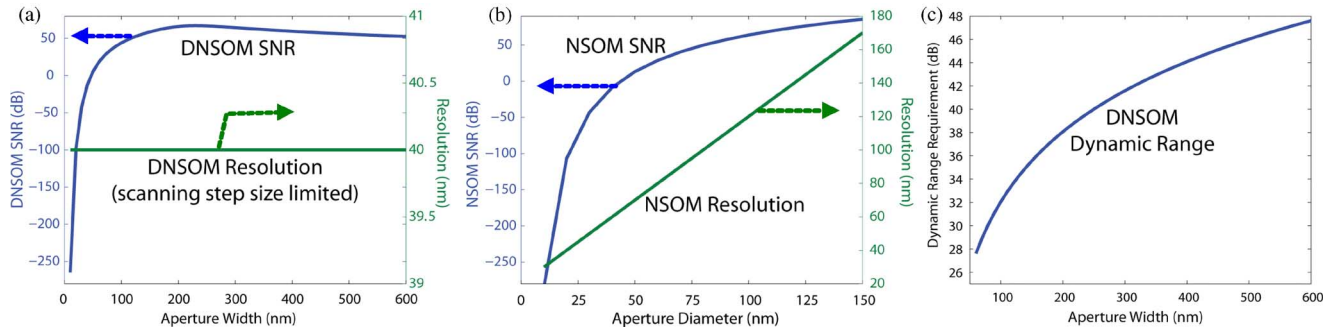

Fig. 2. (a) SNR and resolution as a function of W for DNSOM for a scanning step size of 40 nm. In principle, the spatial resolution can be reduced down to ~7–10 nm with a smaller scanning step size. (b) SNR and resolution as a function of the aperture width for conventional aperture-type NSOM. Notice that for a spatial resolution of <50 nm, the SNR for NSOM rapidly decreases, whereas DNSOM can achieve such a high spatial resolution with an SNR of >50 dB. (c) The dynamic range requirement for DNSOM as a function of the aperture width.

aperture/detectorfour replicas of the original object function $O(x, y)$ are recovered. Each replica is centered on one of the corners of the square.

Therefore, since the scanning step size can be made to be less than a nanometer with the current state-of-the-art piezoelectric scanners, we can conclude that the spatial resolution of the DNSOM practically depends only on the sharpness of the corners of the square structure. In the derivation of (2), corners of the square were assumed to be ideal, as defined by $\mathrm{Rect}(x, y)$, i.e., after 2-D differentiation, each corner yields a 2-D Dirac-delta function, $\delta(x, y)$. For an imperfect square with slightly round corners [where $\mathrm{Rect}(x, y)$ can no longer perfectly define the DNSOM aperture], after 2-D differentiation, each corner of the square will yield a point-spread function, $c(x, y)$, where $c(x, y) \neq \delta(x, y)$. Each replica image will, therefore, be equal to the convolution of the true object function with the point-spread function, i.e., $O(x, y) \otimes c(x, y)$. Since the $\partial^2/\partial x' \cdot \partial y'$ operator creates a narrower point-spread function than the actual geometrical corner roundness, the use of focused-ion-beam milling or electron-beam writing could, in principle, result in a DNSOM point-spread function narrower than ~10 nm. A similar discussion also applies to the skin depth $(L_s)1$ of the optical field at the square edges. In conventional NSOM, the lower bound of the effective aperture diameter is roughly $2L_s$, whereas, in DNSOM, the limiting effect of the skin depth is reduced to $\sim L_s$, since each of the sidewalls of the square operates separately.

The width (W) of the square aperture/detector in the DNSOM affects two quantities: 1) the maximum area of the object that can be imaged and 2) the light throughput. The field-of-view (FOV) area for the DNSOM with a square aperture is $2\,W \times 2\,W = 4\,W^2$. In order to avoid irreparable information loss, the object should be smaller than $2\,W$ in either dimension [39]. For flat samples, a larger FOV can be achieved using, in parallel to the scanning DNSOM aperture/detector, a moveable rectangular mask that has an area of $2\,W \times 2\,W$. This way, by translating the mask by $2\,W$ along x and/or y, new regions on the large object surface can be scanned using the DNSOM.

In terms of light throughput, there is an exponential penalty as the width is reduced in the region $W << \lambda$. For the other limiting case of $W >> \lambda$, the transmission of the square aperture increases as $\sim W^2$. In between these two regions $(W \sim \lambda)$, the ratio of the effective transmission area to the real physical area of a small hole approaches unity and the light throughput penalty is minimized. However, as illustrated in Fig. 2(a), enlarging the square-aperture size beyond, e.g., 200–300 nm does *not* increase the SNR of the DNSOM since the light throughput is already quite close to unity. As W is further increased (e.g., >300 nm), relative intensity noise and shot noise start to reduce the overall SNR of the DNSOM. This SNR reduction for $W > 300$ nm, on the other hand, is not a severe one since it drops quite smoothly yielding an SNR > 50 dB even for $W \approx 600$ nm. A comparison of the SNR and the resolution behavior of the DNSOM versus the conventional NSOM is given in Fig. 2(a) and Fig. 2(b), respectively, illustrating that the DNSOM can achieve a spatial resolution of, e.g., ~40 nm with an SNR of >50–70 dB [see Fig. 2(a)], whereas, for achieving such a high spatial resolution, a conventional aperture-type NSOM system would have to be severely limited by a poor SNR of <-40 dB [see Fig. 2(b)]. This poor SNR behavior of conventional aperture-type NSOM systems is directly related to the fact that as the aperture diameter is reduced below 50 nm, there is an exponential transmission penalty for the probe. *Therefore, the DNSOM can improve the SNR of a conventional NSOM system by* ~100 dB *especially at spatial resolution levels of* <50 nm*, which is a very promising step toward achieving reliable and repeatable imaging of biological specimens with a resolution of* <50 nm *using aperture-based near-field microscopy.* One should emphasize here that the spatial resolution of Fig. 2(a) was chosen to be limited by the scanning step size. In principle, a resolution equal to a single skin depth ($L_s \sim$ 7–10 nm) is feasible with the DNSOM.

The upper bound of W in the DNSOM is governed by the *dynamic range* of the detection system. Fig. 2(c) illustrates that the DNSOM requires a detector with a dynamic range of <50 dB for $W \leq 600$ nm, which is quite a reasonable requirement for the current state of photon counting detectors such as avalanche photodiodes.

B. Experimental Proof-of-Principle of DNSOM

In order to experimentally verify the improved performance of the DNSOM, we used the near-field scanning setup shown in Fig. 1(a). For this proof-of-principle experiment, using a

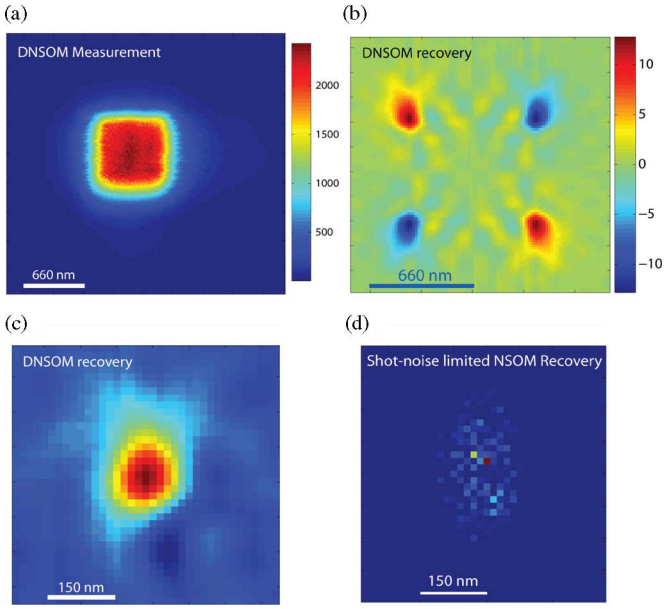

Fig. 3. (a) DNSOM measurement result acquired using the experimental setup, shown in Fig. 1(a). Fig. 1(b) 2-D spatial derivative of the DNSOM measurement results in four recovered images, each one of which is centered around one corner of the DNSOM aperture. Fig. 1(c) The final DNSOM recovery result obtained by combining the information from all four corners, showing the near-field emission pattern of a 100-nm wide NSOM tip, shown in Fig. 1(b). The spatial resolution is ∼40 nm. Fig. 1(d) Shot-noise limited recovery result of aperture-type NSOM for the same object.

wide-square DNSOM aperture [Fig. 1(c)], we imaged the near-field intensity distribution of a 100-nm wide commercially available NSOM tip [Fig. 1(b)] with a spatial resolution of ∼40-nm. This initial experiment is significant for two reasons: 1) *it experimentally verifies the concept of DNSOM by achieving* ∼40-nm *spatial resolution with high SNR and contrast* and 2) *it provides a direct comparison between the conventional aperture-type NSOM and DNSOM, since, in this experiment, using DNSOM, we imaged the near-field of a commercially available NSOM tip*. To give an analogy, this initial experiment is similar to an SEM system imaging the tip of a commercially available AFM, i.e., since the SEM has better spatial resolution than the AFM, it can easily image the fine features of an AFM tip. In a similar way, the success of the proposed experiment provides a direct comparison between the DNSOM and aperture-type NSOM in terms of spatial resolution.

In this proof-of-principle experiment, a conventional aperture-type NSOM system (Witec, Alpha-SNOM) was used to scan the DNSOM aperture across the NSOM tip [Fig. 1(a)]. Illumination of the NSOM tip was at 532 nm (linearly polarized before hitting the backaperture of the cantilever), and the tip was kept in the near-field of the square aperture using the ac feedback (tapping) mode. The scanning step size was ≈16 nm and the total range of scan was 4.2 μm × 4.2 μm. The transmitted light through the DNSOM aperture was collected by an inverted confocal microscope and detected by a photomultiplier tube. Fig. 3(a) shows the DNSOM image that was obtained by measuring the power transmitted through the square aperture as it was scanned over the NSOM tip. Fig. 3(b) shows the result of the

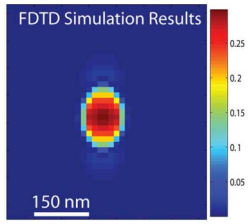

Fig. 4. FDTD simulation of the near-field distribution of a 100-nm aperture on a planar aluminum film. The measurement results presented in Fig. 3(c) are in fairly good agreement with the shown FDTD simulation results.

2-D derivative operation applied to the DNSOM measurement, resulting in four independent recoveries of the near-field intensity of the 100-nm-wide NSOM aperture, shown in Fig. 1(b). Each recovery, centered on one of the corners of the DNSOM aperture, was, then, added to provide the final DNSOM image [Fig 3(c)], which shows the near-field emission pattern of the NSOM probe of Fig. 1(b). Overall, the recovery result agrees well with the physical size of the tip aperture (≈100 nm), where, including the skin depth (∼10 nm), the effective aperture diameter becomes ≈120 nm. Furthermore, the results are also in fairly good agreement with a finite-difference time-domain (FDTD) simulation of the near-field distribution of a 100-nm hole opened on a 150-nm thick aluminum plane (Fig. 4). For this FDTD simulation, the illumination light is assumed to be a plane wave with linear polarization at 532 nm. We did not observe a major asymmetry between the x- and y-directions in our experimental results [Fig. 3(c)], possibly because the polarization of the beam exiting the NSOM tip was not well defined in our experiment due to the pyramidal geometry of the tip. *The experimental recovery result presented in* Fig. 3(c) *showed a spatial resolution of* ∼40 nm *demonstrating the proof-of-principle of the DNSOM*. To provide a direct comparison, Fig. 3(d) shows the shot-noise-limited behavior of an aperture-type NSOM system for imaging the same object at a resolution of ∼40 nm. This unacceptable recovery [Fig. 3(d)] of the conventional aperture-type NSOM system is a direct consequence of its poor SNR behavior at such high-resolution levels, as also highlighted in Fig. 2(b).

In summary, we have illustrated the proof-of-principle of a new near-field optical microscopy approach (DNSOM) that can achieve a spatial resolution of <50 nm with a significantly enhanced SNR performance. We can summarize important advantages of DNSOM as follows. 1) The resolution of the image is not limited by the size of the aperture, but, rather, it is practically limited by the sharpness of the corners of the aperture. This feature of DNSOM may be particularly relevant because it is easier to fabricate sharp corners in a relatively large aperture (or detector) than to fabricate small-area apertures/detectors. 2) The light throughput (and, therefore, the SNR) is significantly increased since the DNSOM does not require an aperture diameter of <100 nm to achieve nanometer-level resolution. 3) Low-power damage threshold of the conventional small-area NSOM probes should be improved with the larger area of a DNSOM aperture. This implies a further increase in the SNR since one can increase the illumination power without damaging

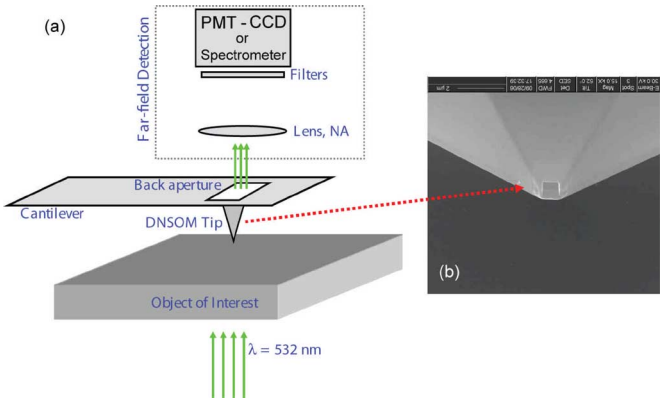

Fig. 5: (a) Schematic of the experimental setup for DNSOM and DNSOM^2. (b) SEM image of a square-DNSOM tip fabricated on a hollow pyramidal tip using focused ion beam milling.

the DNSOM probe. 4) DNSOM opens up the possibility of scanning a relatively large square-area detector (or an array of detectors) in the near-field of an object to achieve nanometer-resolution imaging. This characteristic of the DNSOM may permit the detection of the near-field intensities in the near-field, avoiding complexities and spatial frequency information mixing that occur when transferring the near-field information to far-field detectors. 5) The limiting effect of the skin depth on resolution is improved, i.e., in a small-area aperture, the lower bound of the effective aperture width is roughly 2 L_s, whereas, in DNSOM, the same limiting effect of the skin depth is reduced to $\sim L_s$.

III. Further Improvement of Differential NSOM Using a Sensor Array: DNSOM^2

A. Theory behind DNSOM^2

In the previous section, we illustrated the proof-of-principle of a new near-field optical microscopy approach (DNSOM) that can achieve ultrahigh spatial resolution beyond the diffraction limit (e.g., <50 nm) with a significant improvement in the SNR (e.g., ~100 dB). In this section, we will introduce a variation of the DNSOM to further improve the SNR of our differential near-field imaging system. For this purpose, we aim to replace the confocal-based photon counting scheme of Fig. 1(a) with an inverted sensor array configuration, i.e., instead of counting photons as a function of the scanning position, this new technique will record a frame/image per each scanning position using, e.g., a highly sensitive charged-coupled device (CCD) [see Fig. 5(a)]. We refer to this technique as DNSOM^2 since multiple images of the near-field interaction of the probe with the sample are recorded in DNSOM^2. *While* DNSOM^2 *shares all the advantages of DNSOM listed in the previous section, this new imaging scheme of* DNSOM^2 *allows a further increase in SNR of the near-field images, as will be discussed next.*

DNSOM^2 relies on the fact that the transmitted/collected light through a DNSOM^2 aperture at each scanning position will be large enough to put *each* individual pixel of sensor array into its shot-noise regime. This condition is quite difficult to achieve for conventional aperture-type NSOM systems due to their poor SNR performance at a resolution level of <50 nm [see, e.g., Fig. 3(d)]. As a result of this, such an array of detectors cannot be used (without significant averaging) in NSOM, since each individual element of the detector array will, then, be dominated by noise. The comparative behavior of DNSOM^2 and DNSOM is intuitively analogous to the difference between frequency-domain and time-domain OCT systems.

The recorded quantity in DNSOM^2 is a 4-D data structure, and similar to (1), *for spatially incoherent imaging*, one can write the detected quantity as

$$P(x', y', x, y) = [O(x, y) \cdot \mathrm{Rect}(x - x', y - y')] \otimes h(x, y) \tag{3}$$

where (x, y) defines the real space of each CCD image, and (x', y') defines the shift space of the DNSOM probe. Since both $O(x, y)$ and $h(x, y)$ are nonnegative real quantities for all (x, y) values, the detected image per each scanning position will also be nonnegative, such that there is *no* need for a phase recovery step for incoherent imaging (e.g., for fluorescently labeled sample imaging). However, for *spatially coherent imaging,* the situation is slightly more complicated since (3) must now be rewritten as

$$P(x', y', x, y) = |[o(x, y) \cdot \mathrm{Rect}(x - x', y - y')] \otimes p(x, y)|^2 \tag{4}$$

where $h(x, y) = |p(x, y)|^2$ and $O(x, y) = |o(x, y)|^2$. Equation (4) indicates that if the spatial coherence condition is met, the phase information of $[o(x, y) \cdot \mathrm{Rect}(x - x', y - y')] \otimes p(x, y)$ is lost due to intensity detection at the far-field. However, for amplitude objects where $o(x, y)$ is real, this unknown phase at each data point (x', y', x, y) can only take discreet values of either 0 or π. Hence, the phase ambiguity can easily be removed using well-known phase recovery approaches by iterating back and forth in the (x, y) image and Fourier transform planes [46]. Therefore, for amplitude objects

$$P_R(x', y', x, y) = [o(x, y) \cdot \mathrm{Rect}(x - x', y - y')] \otimes p(x, y) \tag{5}$$

can be recovered by iterative processing of (4). A direct comparison between (3) and (5) indicates that both incoherent and coherent DNSOM^2 systems effectively yield similar detected quantities.

For the sake of simplicity, we proceed with the derivation of DNSOM^2 under a coherent imaging condition. To achieve recovery of the object function $O(x, y) = |o(x, y)|^2$, we take a 2-D spatial derivative of $P_R(x', y', x, y)$ [i.e., (5)] along (x', y'), followed by a 2-D Fourier transform along (x, y), such that: $D(x', y', f_x, f_y) = FT_{(x,y)}\{\frac{\partial^2 P_R(x', y', x, y)}{\partial x' \cdot \partial y'}\}$, where $FT_{(x,y)}\{\ldots\}$ stands for the 2-D Fourier transform operation along (x, y), and f_x and f_y stand for spatial frequencies along x and y, respectively. Similar to the DNSOM, the general expression for $D(x', y', f_x, f_y)$ permits unique recovery of $O(x, y) = |o(x, y)|^2$ for an entire field-of-view of $2\,W \times 2\,W = 4\,W^2$. In order to derive a simpler and more intuitive expression, we can expand $|D(x', y', f_x, f_y)|$ for an object size that is smaller

than W (i.e., the size of the square aperture) as

$$|D(x',y',f_x,f_y)| = \begin{bmatrix} |o(x'-W/2,\ y'-W/2)| \\ +|o(x'+W/2,\ y'+W/2)| \\ -|o(x'+W/2,\ y'-W/2)| \\ -|o(x'-W/2, y'+W/2)| \end{bmatrix} \cdot Circ(f_x,f_y) \quad (6)$$

where

$$\mathrm{Circ}(f_x,f_y) = \mathrm{FT}_{(x,y)}p(x,y) = \left\{ \begin{array}{l} 1,\ if\sqrt{f_x^2+f_y^2} < \mathrm{NA}/\lambda \\ 0,\ \text{elsewhere} \end{array} \right\}$$

and NA (e.g., 0.9) is the effective NA of the far-field imaging system [see Fig. 5(a)].

To understand the similarities and differences between DNSOM and DNSOM^2, a comparison between (2) and (6) is very useful. *Both of these differential near-field techniques create four replicas of the original function centered on each corner of the square aperture, and the sharper the corners of the aperture, the higher the spatial resolution.* However, since DNSOM^2 has a 4-D data structure, it achieves parallel multiple recoveries of $O(x,y) = |o(x,y)|^2$, all at the same time. As evident from (6), for each (f_x, f_y) pair that satisfies the $\sqrt{f_x^2+f_y^2} < \mathrm{NA}/\lambda$ condition, we get *an independent recovery* of $O(x,y) = |o(x,y)|^2$. A similar recovery result could also be obtained for the incoherent imaging case of (3), illustrating the fact that DNSOM^2 can achieve massive parallel imaging of the near-field of an object within the same data acquisition time of either DNSOM or NSOM.

The SNR improvement of DNSOM^2 with respect to DNSOM can be computed using (6) as $\pi \cdot \mathrm{NA}^2 \cdot W^2/\lambda^2$. Assuming $W = 1000$ nm, NA $= 1.4$, and $\lambda = 500$ nm for DNSOM^2, one can compute an SNR increase of $\sim$25-fold over DNSOM. *We should note here that this improvement of 25-fold is over the performance of the DNSOM, which itself improves the SNR of the near-field image by* $\sim$100 dB *at a resolution level of* $<$50 nm, *as illustrated in the previous section.*

B. Experimental Proof-of-Principle of DNSOM^2

In order to provide a proof-of-principle of DNSOM^2, we used the experimental setup shown in Fig. 6(a), where a cooled CCD camera (Q-Imaging, RetigaFast) imaged the near-field interaction of a square DNSOM^2 aperture ($W \sim 1000$ nm) with the object of interest through a far-field NA $= 1.4$. In this experiment, the object was a standard NSOM cantilever, the tip of which was modified using focused ion beam (FIB) milling into the shape of a rectangle, i.e., the near-field mode profile of this rectangular aperture [see Fig. 6(b)] was our object of interest. The illumination wavelength was chosen to be 633 nm.

Processing the recorded DNSOM^2 data [as discussed earlier in (6)], we recovered the near-field intensity profile of the rectangular aperture at the tip of the cantilever, as shown in Fig. 6(c). The results indicated a two-lobed emission pattern, which partially fills the long axis of the rectangle. In order to theoretically

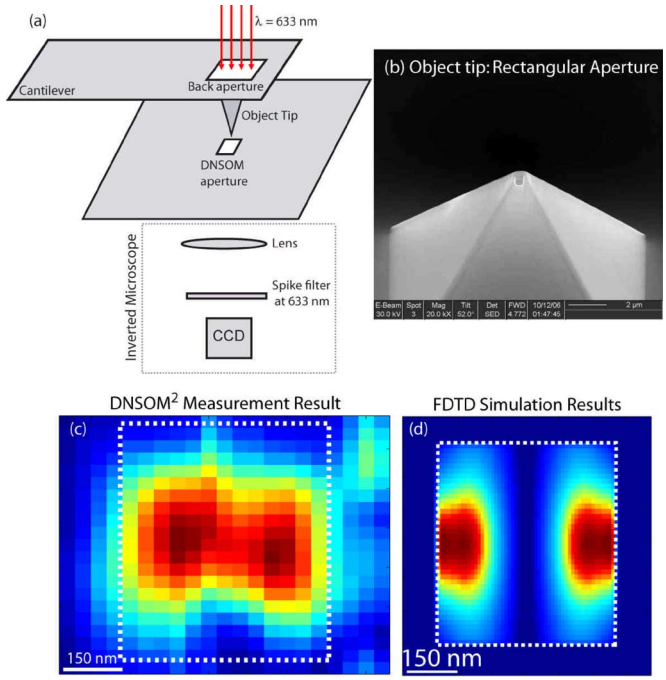

Fig. 6. (a) DNSOM^2 proof-of-principle experimental setup. (b) SEM image of the rectangular object tip. (c) DNSOM^2 measurement results. (d) 2-D FDTD simulation results for the rectangular aperture, shown in Fig. 6(b). White dashed frames in (c) and (d) indicate the boundaries of the rectangular aperture of Fig. 6(b).

verify this observed behavior, we did an FDTD simulation for the same size of the rectangular aperture, the results of which also indicated a two-lobed structure partially filling the long axis of the rectangle [see Fig. 6(d)], further validating the concept of DNSOM^2. The discrepancies between our DNSOM^2 measurement results and the FDTD simulation results can be attributed to the fact that in our theoretical modeling we assumed a 2-D structure for the rectangular aperture to simplify the computation requirements, and, therefore, ignored the 3-D pyramidal structure of the tip, shown in Fig. 6(b).

IV. Further Design Issues in DNSOM and DNSOM^2

It is critical to transform the initial proof-of-principle experimental setups of DNSOM and DNSOM^2 [shown in Figs. 1(a) and 6(a), respectively] into a more flexible design. In these proof-of-principle experiments, we used a *planar* square-DNSOM aperture [Fig. 1(c)] placed onto a scanning stage and the object of interest is placed onto the tip of a cantilever. This initial approach can still be used for certain samples that can be attached to the tip of a cantilever; however, this is quite limiting, in general, for larger samples that cannot be easily attached to a cantilever. To be able to work with any sample, in general, we plan to fabricate square-DNSOM apertures at the tip of a standard hollow pyramidal cantilever, such that we can place any object of interest onto the scanning stage, as shown in Fig. 5(a). One example of such a DNSOM square aperture that we fabricated using FIB milling is illustrated in Fig. 5(b). In the experimental configuration of Fig. 5(a), different than

Figs. 1(a) and Figs. 6(a), the sample will be scanned, while the DNSOM square probe will be kept stationary in the near-field of the object.

Fig. 5(a) illustrates a collection-mode operation for DNSOM/DNSOM^2, where the square aperture located at the tip of the cantilever is just used to collect the transmitted near-field intensity of the sample. Different than the collection mode, for an illumination mode, the function of the square aperture is to locally illuminate the sample, and an inverted microscope can be used to collect the transmitted light delivered through the square aperture of the tip. The illumination mode of operation can be more convenient to operate experimentally since inverted microscopes are readily available, that can easily be integrated with AFM scanning systems. However, in order to convert the near-field setup, shown in Fig. 5(a) into an illumination mode, a different probe geometry is required. The pyramidal geometry of Fig. 5(b) is not suitable for the illumination mode, since it will cut off most of the higher spatial modes of the square aperture, yielding a rounded modal profile for the illumination. In order to prevent this sharpness loss problem for the illumination mode, a probe that has a width much larger than the square aperture is needed, such that all the higher-order modes of the square region can be simultaneously excited. This modification complicates the design of the square-aperture probe, and that is why the collection mode of operation depicted in Fig. 5(a) is one preferred solution.

We should also mention that as a result of the relatively large width of the DNSOM/DNSOM^2 aperture (e.g., $W \sim 200$–600 nm), the resolution of the simultaneous AFM image obtained by the near-field probe (which normally complements the near-field image) will be degraded. This can especially be an issue for imaging deep structures of an object where the probe will not be able to fit. To partially solve this problem, a small metallic tip can be fabricated to the side of the DNSOM aperture, to yield better complementary AFM images, which will also help the DNSOM/DNSOM^2 probe remain in the near-field of a given object for all the scanning positions.

For DNSOM^2 to significantly improve the SNR of the obtained image, we need a high-NA lens since the SNR improvement of DNSOM^2 over DNSOM is given by: $\pi \cdot \mathrm{NA}^2 \cdot W^2/\lambda^2$. However, the short working distance of most high-NA objectives can be an issue in terms of space, since the back of the cantilever also needs to have some free space for the reflection spot of the stabilization laser. To address this space issue, we can use long working distance high-NA objective lenses, which will have >0.6 cm of working distance providing enough room for regular operation of the cantilever and the stabilization laser. This space issue is less problematic for the DNSOM since it does not require a high- NA lens [see (2)]. For DNSOM, we can use less-expensive low-NA objective lenses and achieve the regular performance of the apertured cantilever.

For DNSOM and DNSOM^2 to reach a very high spatial resolution of the order of a single skin depth ($\sim$10 nm), the scanning stage needs to have a step size smaller than 10 nm, e.g., 4 nm. This implies that for a field-of-view of 1 μm $\times$ 1 μm, a total of 250×250 points need to be sampled for DNSOM/DNSOM^2. For even a slow scanning speed of 1 μm/s, this implies an image acquisition time of $\sim$4 min. When compared with other high-resolution imaging modalities [5], this is a reasonable period of time during which the sample has to remain free from external perturbations. For some applications, where, e.g., the Brownian motion of the object will be a limiting factor on the image quality, a faster scanning speed can be used to partially cancel the effect of such uncontrolled motion of the object. Since DNSOM and DNSOM^2 have significantly improved SNR, a higher scanning speed at the cost of some reduction in the overall SNR of the system can be tolerated.

For DNSOM^2, 250×250 data points imply a total of 62 500 frames to be collected within the entire image acquisition time. For this purpose, a fast digital camera (e.g., Hamamatsu C9100) with an acquisition speed of $>$250 frames/s is needed. Assuming an optical magnification of 140 times, and a pixel size of 10 μm at the CCD camera, the digital size of each frame will be $<$15 KB, implying a total DNSOM^2 data size of $\sim$10 GB, which is quite reasonable for the current state-of-the-art computer systems. This entire $\sim$10 GB worth of DNSOM^2 data will be processed, according to (6), to recover the near-field image of the sample with a significantly enhanced SNR.

V. Conclusion

In summary, we have illustrated the proof-of-principles of two new near-field optical microscopy modalities (DNSOM^2 and DNSOM) that can achieve a spatial resolution of $<$50 nm with a significantly enhanced SNR performance. DNSOM and DNSOM^2 share some common important advantages such as: 1) significantly improved SNR (e.g., $>$100 dB); 2) ease of fabrication of large area probes; 3) increased optical power damage threshold for the probe; and 4) reduction in the limiting effect of the skin depth on spatial resolution.

Acknowledgment

We would like to acknowledge M. Kress of Witec for his outstanding technical support.

References

[1] M. A. Schwentker, H. Bock, M. Hofmann, S. Jakobs, J. Bewersdorf, C. Eggeling, and S. W. Hell, "Wide-field subdiffraction RESOLFT microscopy using fluorescent protein photoswitching," *Microsc. Res. Tech.*, vol. 70, pp. 269–280, 2007.

[2] E. Betzig, P. L. Weiner, and J. S. Weiner, *Appl. Phys. Lett.*, vol. 60, p. 2484, 1992.

[3] A. Lewis, M. Isaacson, A. Harootunian, and A. Muray, *Ultramicroscopy*, vol. 13, p. 227, 1984.

[4] D. W. Pohl, W. Denk, and M. Lanz, *Appl. Phys. Lett.*, vol. 44, p. 651, 1984.

[5] L. Novotny and B. Hecht, *Principles of Nano-Optics*. New York: Cambridge University Press, 2006.

[6] U. C. Fischer, *J. Vac. Sci. Technol. B.*, vol. 3, p. 386, 1985.

[7] E. Betzig, A. Lewis, A. Harootunian, M. Isaacson, and E. Kratschmer, *Biophys. J.*, vol. 49, p. 269, 1986.

[8] E. Betzig, J. K. Trautman, T. D Harris, J. S. Weiner, and R. L. Kostelak, *Science*, vol. 251, p. 1468, 1991.

[9] E. Betzig and R. J. Chichester, *Science*, vol. 262, p. 1422, 1993.

[10] Y. Inouye and S. Kawata, *Opt. Lett.*, vol. 19, p. 159, 1994.

[11] P. Ephrat, K. Roodenko, K. L. Nagli, and A. Katzir, *Appl. Phys. Lett.*, vol. 84, p. 637, 2004.

[12] A. Rasmussen and V. Deckert, *Anal. Bioanal. Chem.*, vol. 381, p. 165, 2005.
[13] T. Mitsui, *Rev. Sci. Instrum.*, vol. 76, p. 043703, 2005.
[14] Q. Gan *et al.*, *Appl. Phys. Lett.*, vol. 88, p. 121111, 2006.
[15] B. Bailey, D. L. Farkas, D. L. Taylor, and F. Lanni, "Enhancement of axial resolution in fluorescence microscopy by standing-wave excitation," *Nature*, vol. 366, pp. 44–48, 1993.
[16] T. A. Klar, E. Engel, and S. W. Hell, "Breaking Abbe's diffraction resolution limit in fluorescence microscopy with stimulated emission depletion beams of various shapes," *Phys. Rev. E Stat. Nonlinear Soft Matter Phys.*, vol. 64, p. 066613, 2001.
[17] A. V. Failla, A. Cavallo, and C. Cremer, "Subwavelength size determination by spatially modulated illumination virtual microscopy," *Appl. Opt.*, vol. 41, pp. 6651–6659, 2002.
[18] T. P. Burghardt, K. Ajtai, and J. Borejdo, "*In situ* single-molecule imaging with attoliter detection using objective total internal reflection confocal microscopy," *Biochemistry*, vol. 45, pp. 4058–4068, 2006.
[19] S. T. Hess, T. P. Girirajan, and M. D. Mason, "Ultra-high resolution imaging by fluorescence photoactivation localization microscopy," *Biophys. J.*, vol. 91, pp. 4258–42572, 2006.
[20] M. J. Rust, M. Bates, and X. Zhuang, "Sub-diffraction-limit imaging by stochastic optical reconstruction microscopy (STORM)," *Nat. Methods*, vol. 3, pp. 793–795, 2006.
[21] F. Keilmann and R. Hillenbrand, *Phil. Trans. R. Soc. Lond. A*, vol. 362, p. 787, 2004.
[22] M.R. Speicher, S.G. Ballard, and D. C. Ward, *Nat. Genet.*, vol. 12, p. 368, 1996.
[23] Y. Matsuda, and V.M. Chapman, *Electrophoresis*, vol. 16, p. 261, 1995.
[24] K. Konig, *J. Microsc.*, vol. 200, p. 83, 2000.
[25] S. M. Nie and R. N. Zare, *Annu. Rev. Biophys. Biomol. Struct.*, vol. 26, p. 567, 1997.
[26] J. Hwang, L. A. Gheber, L. Margolis, and M. Edidin, "Domains in cell plasma membranes investigated by near-field scanning optical microscopy," *Biophys. J.*, vol. 74, pp. 2184–2190, 1998.
[27] J. D. Bui, T. Zelles, H. J. Lou, V. L. Gallion, M. I. Phillips, and W. Tan, "Probing intracellular dynamics in living cells with near-field optics," *J. Neurosci. Methods*, vol. 89, pp. 9–15, 1999.
[28] H. Shiku and R. C. Dunn, "Domain formation in thin lipid films probed with near-field scanning optical microscopy," *J. Microsc.*, vol. 194, pp. 455–460, 1999.
[29] F. de Lange, A. Cambi, R. Huijbens, B. de Bakker, W. Rensen, M. Garcia-Parajo, N. van Hulst, and C. G. Figdor, "Cell biology beyond the diffraction limit: Near-field scanning optical microscopy," *J. Cell Sci.*, vol. 114, pp. 4153–4160, 2001.
[30] M. Hausmann, B. Perner, A. Rapp, L. Wollweber, H. Scherthan, and K. O. Greulich, "Near-field scanning optical microscopy in cell biology and cytogenetics," *Methods Mol. Biol.*, vol. 319, pp. 275–294, 2006.
[31] A. Cricenti, R. Generosi, M. Luce, P. Perfetti, G. Margaritondo, D. Talley, J. S. Sanghera, I. D. Aggarwal, N. H. Tolk, A. Congiu-Castellano, M. A. Rizzo, and D. W. Piston, "Chemically resolved imaging of biological cells and thin films by infrared scanning near-field optical microscopy," *Biophys. J.*, vol. 85, pp. 2705–2710, 2003.
[32] F. J. Garcia deAbajo, *Opt. Express*, vol. 10, p. 1475, 2002.
[33] H. A. Bethe, *Phys. Rev.*, vol. 66, p. 163, 1944.
[34] X. Heng, D. Erickson, P. Demetri, and Y. Changhuei, in *Proc. SPIE.*, 2005, vol. 6003, p. 40.
[35] F. Zenhausern, Y. Martin, and H. K. Wickramasinghe, *Science*, vol. 269, p. 1083, 1995.
[36] B. Knoll and F. Keilmann, *Nature*, vol. 399, p. 134, 1999.
[37] T. J. Yang, G. A. Lessard, and S. R. Quake, *Appl. Phys. Lett.*, vol. 76, p. 378, 2000.
[38] A. Barbara, T. Lopez-Rios, and P. Quemerais, *Rev. Sci. Instrum.*, vol. 76, p. 023704, 2005.
[39] A. Ozcan, E. Cubukcu, A. Bilenca, K. B. Crozier, B. E. Bouma, F. Capasso, and G. J. Tearney, *Nano Lett.*, vol. 6, p. 2609, 2006.
[40] "Sharp corners and kaleidoscopes lead to novel microscopy techniques"; *Photon. Spectra*, Jan. Issue, 2007 [Online]. Available: http://www.photonics.com/content/spectra/2007/January/microscopy/86098.aspx
[41] D. Huang *et al.*, *Science*, vol. 254, p. 1178, 1991.
[42] J. M. Schmitt, "Optical coherence tomography (OCT): A review," *IEEE Sel. Topics Quantum Electron.*, vol. 5, no. 4, pp. 1205–1215, Jul–Aug. 1999.
[43] W. Drexler, U. Morgner, F. X. Kartner, C. Pitris, S. A. Boppart, X. D. Li, E. P. Ippen, and J. G. Fujimoto, *Opt. Lett.*, vol. 17, p. 1221, 1999.
[44] R. Leitgeb, C. K. Hitzenberger, and A. F. Fercher, *Opt. Express.*, vol. 8, p. 889, 2003.
[45] J. F. de Boer, B. Cense, B. H. Park, M. C. Pierce, G. J. Tearney, and B. E. Bouma, *Opt. Lett.*, vol. 21, p. 2067, 2003.
[46] A. Ozcan, A. Bilenca, B. E. Bouma, and G. J. Tearney, *Appl. Phys. Lett.*, vol. 89, p. 131124, 2006.

Aydogan Ozcan (M'00) received the Ph.D. degree from the Department of Electrical Engineering, Stanford University, Palo Alto, CA, in 2005.

After a short Postdoctoral Fellowship at Stanford University, he was an Instructor at Harvard Medical School, Boston, MA. He joined the University of California, Los Angeles, in 2007, where he is currently an Assistant Professor of Electrical Engineering with a joint appointment at the Biomedical Engineering IDP, Los Angeles. He is the author or coauthor of more than 60 peer-reviewed research articles in major scientific journals and conferences. He is the holder of seven issued and nine pending U.S. patents for his inventions in nanoscopy, wide-field imaging, nonlinear optics, fiberoptics, and optical coherence tomography.

Dr. Ozcan is a member of the IEEE Lasers and Electro-Optics Society, the Optical Society of America, and the International Society for Optical Engineering.

Ertugrul Cubukcu (S'01) received the B.S. and M.S. degrees in physics from Bilkent University, Bilkent, Ankara, Turkey, in 2001 and 2003, respectively. Currently, he is working toward the Ph.D. degree in applied physics at Harvard University, Cambridge, MA.

He has been engaged in research on negative refraction and superlensing effect in photonic crystals. He is the author or coauthor of more than 20 journal and conference papers. His current research interests include surface plasmon photonics and related semiconductor devices as well as new near-field optical microscopy techniques.

Mr. Cubukcu is a Student Member of the American Physical Society and the Optical Society of America. He has served as a Reviewer for the *Physical Review Letters*, the *Applied Physics Letters*, the *Optics Letters*, the *Optics Express*, and the *Optics Communication*.

Alberto Bilenca received the B. Sc., M. Sc., and Ph.D. degrees from the Department of Electrical Engineering, Technion—Israel Institute of Technology, Haifa, Israel, in 1992, 2001, and 2005, respectively.

He is currently an Instructor at the Harvard Medical School, Boston, MA. He is the author or coauthor of more than 70 manuscripts published in foremost journals and conference proceedings. His current research interests include the field of biophotonics with emphasis on biological and medical imaging.

Dr. Bilenca is an Editorial Board Member of the *Open Electrical and Electronic Engineering Journal*. He was the recipient of numerous awards including the Viterbi Fellowship, the Rothschild Postdoctoral Fellowship, and the European Commission Marie-Curie Award.

Brett E. Bouma received the B.S. degree from Hope College, Holland, MI, in 1986, M.S. degree from Michigan State University, East Lansing, in 1988, and the Ph.D. degree from the University of Illinois, Chicago, in 1993, all in physics.

He was a Postdoctoral Fellow and, subsequently, a Research Scientist at the Massachusetts Institute of Technology, Cambridge, where he was engaged in research on the application of ultrafast laser technology in biology and medicine and, in particular, on the development of optical coherence tomography. Upon leaving MIT, he joined the faculty of Harvard Medical School (HMS), Boston, MA, with a primary laboratory at the Massachusetts General Hospital in the Wellman Laboratories of Photomedicine. He is currently an Associate Professor at the HMS and a member of the Harvard-MIT Division of Health Sciences and Technology, Cambridge, MA. His current research interests include the development and application of novel optical technologies for clinical diagnosis.

Federico Capasso (M'79–SM'85–F'87) received the Doctor of Physics degree (*summa cum laude*) from the University of Rome, Rome, Italy, in 1973.

From 1974 to 1976, he was a Researcher at Fondazione Ugo Bordoni, Rome. He joined Bell Laboratories in 1976, where he held positions of a member of the Technical Staff during 1977–1986, the Department Head during 1986–2000, and the Vice-President for Physical Research during 2000–2002. In 1997, he became a Bell Labs Fellow owing to his scientific contributions. He is currently the Robert Wallace Professor of Applied Physics and Vinton Hayes Senior Research Fellow in Electrical Engineering at Harvard University, Cambridge, MA. He has been engaged in research on the Casimir effect and of the field of surface plasmon photonics, which have opened up new directions in electronics, photonics, mesoscopic physics, and nanotechnology. He is a Co-Inventor of the quantum cascade laser, a fundamentally new light source, which has now been commercialized. More recently, he initiated a new line of research using microelectromechanical systems to investigate the basic physics of Casimir effect and its applications to nanomechanics. He is the holder of more than 40 U.S. patents. He is the author or coauthor of more than 300 papers and has edited four volumes. His current research interests include the quantum design of new artificial materials and devices, known as bandstructure engineering.

Prof. Capasso is a member of the National Academy of Sciences, the National Academy of Engineering, and the American Academy of Arts and Sciences. He is also a Fellow of the Optical Society of America, the American Physical Society, the International Society for Optical Engineering, and the American Association for the Advancement of Science. He was the recipient of numerous awards including the King Faisal International Prize for Science, the IEEE Edison Medal, the Arthur Schawlow Prize in Laser Science, the Wetherill Medal of the Franklin Institute, the RobertWood Prize of the Optical Society of America, the William Streifer Award of the IEEE Laser and Electro-Optic Society, the Rank Prize in Optoelectronics (U.K.), the IEEE David Sarnoff Award in Electronics, the Duddell Medal of the Institute of Physics (U.K.), the Willis Lamb Medal for Laser Science and Quantum Optics, the Materials Research Society Medal, the "Vinci of Excellence" Prize (France), the Welker Memorial Medal (Germany), the New York Academy of Sciences Award, the Newcomb Cleveland Prize of the American Association for the Advancement of Science.

Guillermo J. Tearney received the Ph.D. degree from MTI, Cambridge, MA, in 1997, and the M.D. from Harvard Medical School, Boston, MA, in 1998.

He is currently an Associate Professor in the Department of Pathology, Harvard Medical School, Boston, MA, and at the Wellman Center for Photomedicine at Massachusetts General Hospital, Boston. He is the author or coauthor of more than 200 peer-reviewed articles and his work has been featured on the cover of a variety of prestigious journals, such as *Science*, *Nature*, *Circulation*, *Gastroenterology*, and the *Journal of the American College of Cardiology*. His current research interests include the development and validation of noninvasive optical methods for disease diagnosis, including optical coherence tomography, endoscopic confocal microscopy, speckle imaging, and spectroscopy.